Kumazawa *et al. Earth, Planets and Space* (2017) 69:169
https://doi.org/10.1186/s40623-017-0756-6

Earth, Planets and Space

FULL PAPER Open Access

Measuring seismicity diversity and anomalies using point process models: case studies before and after the 2016 Kumamoto earthquakes in Kyushu, Japan

Takao Kumazawa[1*], Yosihiko Ogata[1,2] and Hiroshi Tsuruoka[2]

Abstract

This paper reviews seismic activity in and around the Kumamoto region before and after the April 16, 2016, Kumamoto earthquake of M7.3 using statistical models such as stationary, two-stage, and non-stationary epidemic-type aftershock sequence (ETAS) models to examine seismicity anomalies. Our findings are summarized as follows. First, most of the earthquake clusters before April 2016 are explained by the stationary ETAS model, except for a few clusters of swarm activity, one of which was remotely induced by the 2011 Tohoku-Oki earthquake (M9). The non-stationary ETAS model describes changes in the rate of background seismicity of swarm activity. Second, we revealed seismic quiescence relative to the stationary ETAS model in the foreshock sequence from the M6.5 earthquake on April 14, 2016, and further in the aftershock activity of the 2000 M5.0 earthquake that occurred in the shallower extension of the M6.5 foreshock zone. Thirdly, the main-fault and two off-fault aftershock clusters of the M7.3 mainshock show different features, caused by static triggering effects of the mainshock and/or effects induced by fault weakening. Finally, the *b*-value increased stepwise over time during the entire period of foreshocks and aftershocks, the reason of which is explained.

Background

The 2016 Kumamoto earthquakes, including the mainshock (M7.3), were a series of shallow, strong earthquakes that occurred at and around 01:25 JST on April 16, 2016 (16:25 UTC on April 15), near Kumamoto City in Kyushu, Japan; the first foreshock (M6.5) occurred at 21:26 JST (12:26 UTC) on April 14, 2016.

Several major earthquakes occurred inland in Kyushu at shallow depths ($\leq$ 30 km) within a 100–200-km radius preceding the 2016 Kumamoto mainshock. In January and April 1975, two events of M6.5 and M6.3 (the Northwest Kagoshima-ken earthquakes) occurred successively at distances of 40 and 65 km, respectively, south of the 2016 Kumamoto mainshock. A shallow M7.0 earthquake occurred in March 2005 (the Fukuoka-ken Seiho-oki earthquake) off the northern coast of Kyushu and 110 km north of the Kumamoto event. More recently, in November 2015, a shallow M7.0 earthquake (the Satsuma-hanto Seiho-oki earthquake) occurred off the west coast of Kagoshima Prefecture, Kyushu, approximately 200 km southwest of the Kumamoto M7.3 earthquake. The aftershock activities of the former and latter M7.0 earthquakes were followed by clear quiescence in the sense that until the 2016 Kumamoto earthquakes, no event of scale M4 or larger occurred for more than 10 years and 3 months, respectively. In addition, the March 11, 2011, M9.0 Tohoku-Oki mega-earthquake occurred approximately 1200 km northeast of the Kumamoto event.

Preceding the Kumamoto earthquakes, shallow background seismicity in and around Kumamoto Prefecture had long been present inland in the Japanese Archipelago (Ogata 2017c). Kumamoto Prefecture lies at the western extension of the Japan Median Tectonic Line, where

*Correspondence: tkuma@ism.ac.jp
[1] The Institute of Statistical Mathematics, Tachikawa, Japan
Full list of author information is available at the end of the article

a system of active faults forks in two directions at the Beppu–Haneyama Fault Zone. Specifically, in April 2016, a series of earthquakes ruptured segments of the Hinagu Fault and the Futagawa Fault to its north; these earthquakes occurred along the southern boundary of the Beppu–Shimabara graben, with epicenters moving from west to east over time.

Therefore, this area is known for its high seismic, volcanic, and geothermal activity and the seismic activity in this region exhibits extremely diverse patterns. To quantitatively illustrate this variety in seismicity, we analyzed microseismicity in the Kumamoto region since 2010, before the occurrence of the first M6.5 foreshock. We then analyzed the foreshock sequence of the M6.5 event until the time of the M7.3 Kumamoto mainshock. We further examined how aftershock activity in the main- and off-fault zones differed regionally. Finally, we evaluated temporal and spatial changes in *b*-values in the sequence throughout the M6.5 foreshock sequence and the M7.3 aftershocks over a 2-week period.

For these analyses, we use the epidemic-type aftershock sequence (ETAS; Ogata 1985, 1988) model and its extended versions (Kumazawa and Ogata 2013; Kumazawa et al. 2016a, b) for a variety of seismicity patterns in addition to a model for the magnitude frequency changes (Ogata 1989; Ogata et al. 1991). For each dataset, we compare the goodness-of-fit of the models for the best fit, as given in the following section.

Models and methods

The ETAS model and its extensions

The dataset $\{(t_i, M_i);\ S < t_i < T\}$ comprises the occurrence times of the completely detected earthquakes in a target interval $[S,\ T]$ associated with their magnitudes. Therefore, the stationary ETAS model (Ogata 1985, 1988, 1989, 1992, 2006a, b; Utsu et al. 1995),

$$\lambda_\theta(t|H_t) = \mu + \sum_{\{i:\ S<t_i<t\}} K_0 e^{\alpha(M_i - M_z)} \Big/ (t - t_i + c)^p, \tag{1}$$

is used as the baseline model, where the five constants μ, K_0, α, c, and p are estimated from each dataset. The parameter μ denotes the background seismicity rate, and the other four parameters control the portion of the seismicity rate triggered by the preceding earthquakes. The uppercase character S is the starting time of the target analysis period to which the model is to be applied, and t_i represents the occurrence time of the ith earthquake associated with a magnitude of M_i that is greater than the cutoff magnitude M_c. The history H_t indicates that both coordinates of such earthquakes occurred before time t. Note that when large earthquakes precede the time S, the history H_t should include the occurrence time and the magnitude records of those large earthquakes. For example, such a history includes the mainshock and aftershocks before time S even if these are incompletely detected.

The simplest alternative model for the case where the stationary ETAS is misfit to a dataset is a two-stage ETAS model that uses different parameter values before and after the change-point time. If we hypothesize a fixed change-point time, this model is compared to the single baseline ETAS model using the Akaike information criterion (AIC; Akaike 1973, 1992). However, if the change-point time is estimated, the goodness-of-fit relative to the baseline ETAS model is compared using a modified version of the AIC (Ogata 1992; Kumazawa et al. 2010) because the maximum likelihood estimate (MLE) of the change-point does not satisfy ordinary large-sample theory (Ogata 1978).

Using X-window-based interactive graphical software for data selection (TSEIS; Tsuruoka 1996) and for the mounted ETAS analyses (XETAS; Tsuruoka and Ogata 2015a, b; Ogata and Tsuruoka 2016), the seismicity in several focal regions was preliminarily explored to determine the fit or misfit of the ETAS model. For the detailed manual and related software source, see Ogata (2006a).

If the extended cumulative curve of the first ETAS model for the earlier period overpredicts the empirical cumulative curve in the second period, we may suspect quiescence relative to the first period (relative quiescence). One of the possible physical reasons for relative quiescence is that the seismogenic source is covered by the stress shadow (Ogata 2006b, 2007, 2011a).

In contrast, relative activation can often be triggered by a major external earthquake occurring outside the focal region at time τ, and the seismicity rate can then be expressed by

$$\lambda_\theta(t|H_t) = \mu + \sum_{\{i:\ S<t_i<t\}} K_0 e^{\alpha(M_i - M_z)} \Big/ (t - t_i + c)^p + K_\tau \Big/ (t - \tau + c_\tau)^{p_\tau}, \tag{2}$$

where the last term represents the triggered rate change caused by the external earthquake occurring at time τ. In the present case, the M7.3 Kumamoto earthquake has a potentially static or dynamic triggering effect (cf., Hill and Prejean 2015) to off-fault activities in the Aso and Oita regions. Furthermore, the 2011 M9 Tohoku-Oki earthquake may have triggered microseismicity in the central Kyushu region prior to the Kumamoto earthquakes.

The non-stationary ETAS model (Kumazawa and Ogata 2013, 2014) extends the ETAS model (Ogata 1985, 1988) to fit transient swarms, including induced seismicity, as discussed by Hainzl and Ogata (2005). The parameters for the background rate μ and the aftershock productivity

K_0 of ETAS model (model (1)) are set to be time-dependent in the non-stationary ETAS model:

$$\lambda_\theta(t|H_t) = \mu(t) + \sum_{\{i:\ S<t_i<t\}} K_0(t_i)e^{\alpha(M_i-M_z)} \Big/ (t - t_i + c)^p, \tag{3}$$

where $\mu(t)$ and $K_0(t)$ are technically characterized by piecewise-linear segments connected at the occurrence times of the earthquakes. For the estimation, occurrence data are inverted into the optimal solutions of $\mu(t)$ and $K_0(t)$ under proper smoothness constraints with the assumption that the aseismic stress and changes in the triggering parameter are both stably estimated using an empirical Bayesian method. Kumazawa and Ogata (2013) justified this estimation procedure using simulated datasets. Furthermore, Kumazawa et al. (2016a, b) derived consistent $\mu(t)$ results for a number of volcanic swarms with another independent approach that employs hourly sampled volumetric stress changes as external records.

The goodness-of-fits of the above extended models are compared based on the increments $\Delta\mathrm{AIC} = \mathrm{AIC} - \mathrm{AIC}_0$ or $\Delta\mathrm{ABIC} = \mathrm{ABIC} - \mathrm{AIC}_0$, where AIC_0 represents the AIC value of the baseline single ETAS model. Note that the baseline ETAS model is the same as that in the case of the reference ETAS model of the non-stationary model. Specifically, when the weights of the constraints are very large, $\mu(t)$ and $K_0(t)$ become the same as the constant values μ and K_0 in model (1), respectively, as the corresponding reference parameter.

The datasets used throughout the present paper are part of the Hypocenter Catalog compiled by the Japan Meteorological Agency (JMA 2017), and the legitimacy for the results of our analyses performed on those datasets is given in Discussion section.

Magnitude frequency distributions

Changes in *b*-values in space and time

Consider the Gutenberg–Richter formula (Gutenberg and Richter 1944):

$$\begin{aligned}\lambda(M) &= P(M < \text{Magnitude} \le M + \mathrm{d}M) \\ &= 10^{a-bM} = A\mathrm{e}^{-\beta M},\end{aligned} \tag{4}$$

with the constants a, b, and $\beta = b \ln 10$. Restricting the range of earthquake sizes such that $M \ge M_c$, we can derive the probability density distribution $f(M|\beta) = \lambda(M)/\Lambda(M_c) = \beta\mathrm{e}^{-\beta(M-Mc)}$, where $\Lambda(M_c) = \int_{M_c}^{\infty} \lambda(M)\mathrm{d}M$ is the expected total number of earthquakes with $M \ge M_c$. The β value in Eq. (4) can depend on location or time such that $\beta(z)$ is a function of location $z = (x, y)$ or time $z = t$. As the maximum likelihood estimate of the b-value is given by the reciprocal of the magnitude average, local changes in the b-values have conventionally been obtained via various kernel methods or moving weighted averages (Smith 1986; Wiemer and Wyss 1997; Wyss et al. 1997; Nanjo et al. 2016).

Here, we consider β in Eq. (4) to be represented by a flexible function of time and/or location using cubic B-spline expansions (Ogata and Katsura 1993; Ogata et al. 1991). Alternatively, for a two-dimensional spatial region, we use a piecewise-linear function defined on the Delaunay tessellated region. The vertices of each Delaunay triangle comprise the epicenter coordinates of the three nearest earthquakes (Delaunay 1934); in particular, in the case of a one-dimensional space or time axis, a continuous piecewise-linear function, or broken line, of occurrence times is included. The coefficients of these functions are given at space or time vertex locations and additional points in the time interval or rectangular region (Ogata 2011b; Ogata et al. 2003). Therefore, the function is uniquely defined based on linear interpolation of the coefficient values, and the characterization of such flexible functions for β requires a set of high-dimensional coefficients θ. In such a case, a penalized log-likelihood (Good and Gaskins 1971),

$$Q(\theta|w) = \ln(\text{likelihood}) - \text{penalty}(\theta|w), \tag{5}$$

describes the trade-off between maximizing the likelihood function $\prod_i \beta_\theta(z_i)\mathrm{e}^{-\beta_\theta(z_i)}$ of θ for the goodness-of-fit to the data and minimizing a penalty function that penalizes fluctuations (roughness) in the piecewise-linear β function. Here, the penalty function is described by an integral of the sum of the squares of the first and second partial derivative functions with a constraining weight vector w that is called the hyperparameter in a Bayesian framework (Akaike 1980; Parzen et al. 1998; Ogata 2017a, b, c). Then, we objectively implement the best selection among the distinct parameterizations for the penalty and tuning of the hyperparameter values. Therefore, the crucial point is the optimal determination of the suitable w for a given dataset. Then, we can obtain the inversion solution $\beta_\theta(.)$ by maximizing $Q(\theta|w)$.

Earthquake detection rates in time

To investigate b-value changes over time, we take account of the low detection rate of the small aftershocks for time spans immediately after the mainshock as well as immediately after major foreshocks and major aftershocks. However, the traditional method, which restricts earthquakes above a certain completely detected magnitude, loses a large amount of data. Accordingly, we want to model the b-value time variation simultaneously with the variations in the detection rates of the earthquakes. Consider a detection-rate function $q(M)$ of earthquakes of magnitude M such that $0 \le q(M) \le 1$. An example of the detection-rate function is the cumulative function of the normal distribution,

$$q(M|m,\sigma) = 1 \Big/ (\sqrt{2\pi}\sigma) \int_{-\infty}^{M} \exp\left\{(x-m)^2 \Big/ 2\sigma^2\right\} \mathrm{d}x, \tag{6}$$

suggested by Ringdal (1975). Here, the parameter m represents the magnitude value at which 50% of earthquakes are detected, and σ relates to the range of magnitudes in which earthquakes are partially observed. For the time series of magnitudes of all detected earthquakes, Ogata and Katsura (1993, 2006) propose that the time-dependent magnitude frequencies of all detected earthquakes can be characterized by an intensity function

$$\lambda(M|\beta(t), m(t), \sigma(t)) \;=\; f(M|\beta(t)) \cdot q(M|m(t), \sigma(t)). \tag{7}$$

To characterize the non-stationarity of the frequency distributions, we assume that the parameters ln $\beta(t)$, ln $m(t)$, and ln $\sigma(t)$ are expressed by flexible functions of time t using the piecewise-linear function (Kumazawa and Ogata 2013, 2014; Kumazawa et al. 2016a). Then, given a dataset of earthquake occurrence times associated with magnitudes (t_i, M_i), we consider the penalized log-likelihood in Eq. (5), where the log-likelihood function is given by

$$\ln L = \sum_i \Big\{ \ln \beta(t_i) - \beta(t_i) M_i + \ln q(M_i|m(t_i), \sigma(t_i)) + \beta(t_i) m(t_i) - \frac{1}{2}\beta(t_i)^2 m(t_i)^2 \Big\} \tag{8}$$

(see Ogata and Katsura 1993), with penalties against the roughness of ln $\beta(t)$, ln $m(t)$, and ln $\sigma(t)$. Therefore, the optimal determination of the hyperparameters for the respective penalties of ln $\beta(t)$, ln $m(t)$, and ln $\sigma(t)$ is crucial to the method. Here, the penalties to the sum of the square differences of ln $\beta_i = \ln \beta(t_i)$, ln $m_i = \ln m(t_i)$, and ln $\sigma_i = \ln \sigma(t_i)$ may work better than the penalty to the integrated square differentials of ln $\beta(t)$, ln $m(t)$, and ln $\sigma(t)$ in cases where the occurrence times $\{t_i\}$ are highly clustered (Ogata 1989). These results can be compared using the Akaike Bayesian information criterion (ABIC; Akaike 1980).

Results

Prior to the Kumamoto earthquakes

We first analyzed the seismicity around the Kumamoto region (Fig. 1a) from 2010 until the 2016 Kumamoto earthquake, where the data of earthquakes of M1.0 and larger were completely detected in the Hypocenter Catalog of the Japan Meteorological Agency (JMA). First, we applied the single ETAS model and the two-stage ETAS model to search for a change-point in the entire period using the XETAS program. The results are listed in Table 1; specifically, the most likely change-point (the MLE) was reached at 1300 days elapsed (around September 2013 with a significantly better fit than the single ETAS model, with the difference ΔAIC given in Table 1; see the black dashed vertical line in Fig. 1).

Furthermore, we examined whether a triggering effect from the 2011 M9.0 Tohoku-Oki earthquake existed in this area. We compared the AIC values between models (1) and (2) for this examination. Even though the triggering effect appears to be small (the red cumulative curve) in Fig. 1, the fitting of model (2) is significantly better (see the AIC values for cutoff magnitudes $M_c = 1.0$ and 1.5 in Table 1) than single ETAS model (1) represented by the green cumulative curve. The red vertical line indicates the occurrence of the 2011 M9.0 Tohoku earthquake, which was more than 1000 km away, at which time seismicity shows slight activation, and single ETAS model (1) accordingly shows a misfit.

Quiescence can still be significant even with higher threshold magnitudes (Fig. 1b–d) at the same change-point at 1300 days elapsed (Table 1).

We then fit the ETAS model to earthquakes of $M \geq 1.0$ in each subregion R1–R8 (Fig. 2a) selected from the total region shown in Fig. 1a. Significant misfits were detected in the R3, R4, R5, and R8 subregions (see Fig. 3); however, no significant anomalies were found elsewhere. The panels in Fig. 2b show that the ETAS model fits well for the R1, R2, R6, and R7 subregions without any indication of relative quiescence. Conversely, the R3–R5 subregions in the Beppu–Shimabara graben, on the northern side of the fault segments that caused the M6.5 and M7.3 ruptures, showed significant misfits (Fig. 3, left panels, and Table 2). The seismic activity in the R8 subregion had little triggering effect from the 2011 M9.0 earthquake and is normally predicted in the ongoing period; however, another type of misfit was shown during the period a few years earlier (see the bottom panels in Fig. 3).

Non-stationary ETAS model (3) was applied to these subregions to examine the characteristics of the parameter changes (Fig. 3, right panels). Here, the parameter $\mu(t)$ suggests possible changes in the seismic incidence rate caused by either static stress changes or fault weakening of the earthquake occurrence field. The parameter $K_0(t_i)$ shows the size of the aftershock productivity of each earthquake and is systematically dependent on the epicenter position of earthquake i occurring at time t_i (Kumazawa and Ogata 2013, 2014; Kumazawa et al. 2016a, b). In particular, in the R3 subregion, an earthquake swarm occurred in March 2011 (right after the 2011 Tohoku-Oki earthquake) and then subsided in April 2012 (at around $t = 800$ days). The parameter $\mu(t)$ changes according to this observation, reflecting the fact that the swarm activity was remotely triggered by

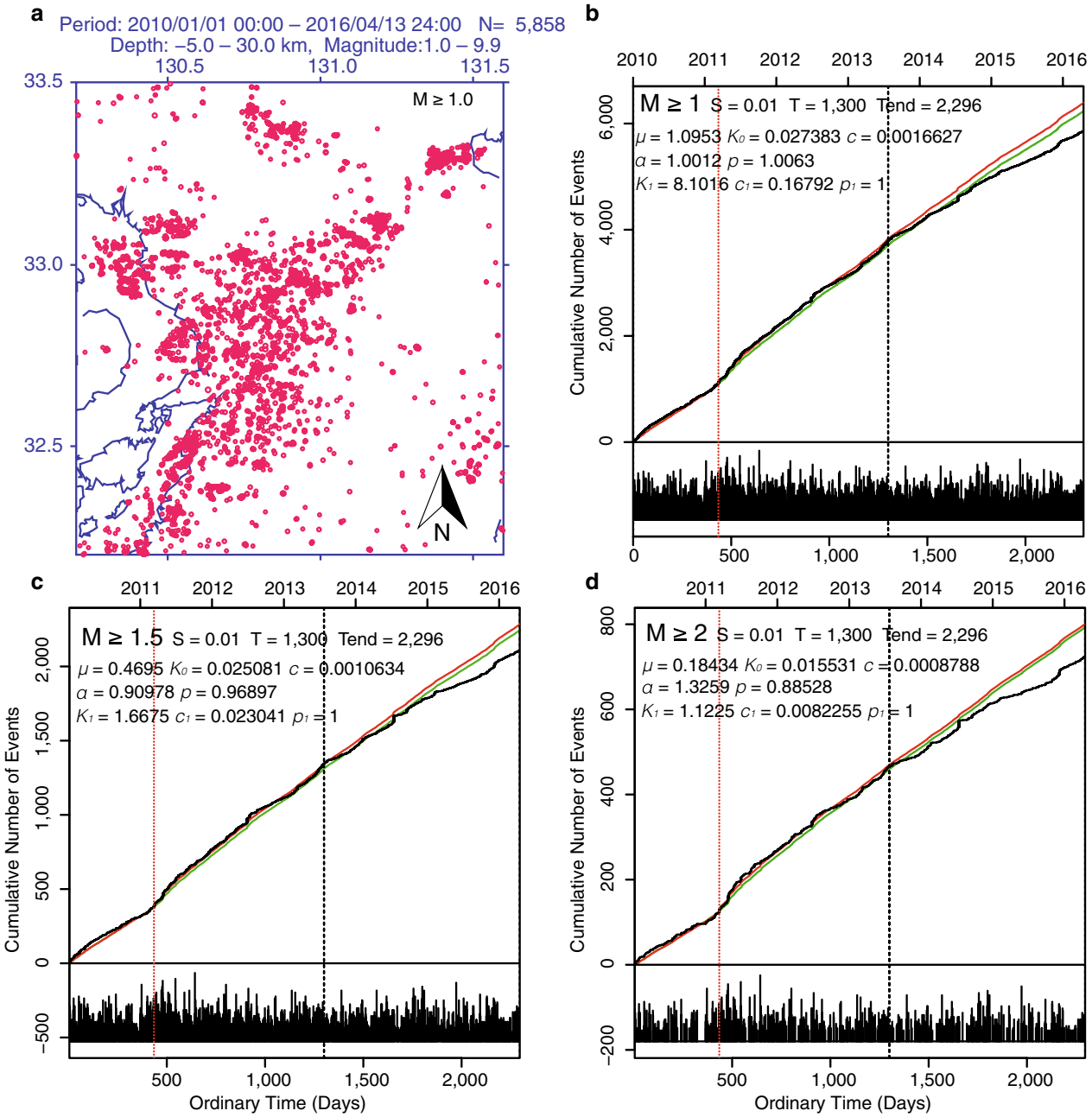

Fig. 1 ETAS model and its extended model estimates. Models (1) and (2) are fit to the seismicity in and around the aftershock region prior to the M6.5 Kumamoto earthquake. **a** Seismicity from 2010 until the M6.5 earthquake with a cutoff magnitude of $M_c = 1.0$. **b**–**d** ETAS models (1) and (2) fitted to the datasets until the change-point (the dashed vertical line) with $M_c = 1.0$, $M_c = 1.5$, and $M_c = 2.0$, respectively. The red vertical lines indicate when the M9.0 Tohoku-Oki earthquake (March 11, 2011) occurred. The green and red cumulative curves of models (1) and (2) are extended for the period until the M6.5 event and are superimposed onto the observed cumulative curve (black curve). The corresponding M–T plots are attached in the bottom sides

the Tohoku-Oki earthquake, which occurred more than 1000 km to the northeast.

In the R4 subregion, several swarms occurred throughout the target period, with the last major one occurring around November 2015 (at around $t = 2200$ days). The R4 and R5 subregions were activated close to when the swarm activity in the R3 subregion subsided; then, these activations ceased in August 2013 (at around

Table 1 Estimated parameters of models (1) and (2) and their respective AIC values

M_c	Model	Period	μ	$K_0(\times 10^{-2})$	$c(\times 10^{-3})$	α	p	$K_\tau(\times 10^{+1})$	$c_\tau(\times 10^{+1})$	p_τ	ΔAIC
1.0	(1)	Total	0.895	2.951	1.226	0.872	1.005	–	–	–	0
		P1	1.063	2.821	1.662	1.005	1.001	–	–	–	− 90.38
		P2	0.552	3.320	0.504	0.625	0.971	–	–	–	
	(2)	Total	0.969	2.620	1.312	0.863	1.033	7.703	5.001	1.0*	− 18.26
		P1	1.095	2.738	1.663	1.001	1.006	0.410	0.0168	1.0*	*− 92.87*
		P2	0.552	3.320	0.504	0.625	0.971	0.000	0.0211	1.0*	
1.5	(1)	Total	0.432	2.541	1.103	0.813	1.008	–	–	–	0
		P1	0.457	2.600	0.106	0.922	0.963	–	–	–	− 29.54
		P2	0.429	2.134	1.068	0.640	1.087	–	–	–	
	(2)	Total	0.450	2.166	1.308	0.772	1.055	4.079	5.302	1.0*	− 12.24
		P1	0.469	2.508	1.063	0.910	0.969	0.168	0.0230	1.0*	*− 31.15*
		P2	0.428	2.134	1.068	0.640	1.087	0.000	0.0223	1.0*	
2.0	(1)	Total	0.183	1.685	0.941	1.099	0.966	–	–	–	0
		P1	0.182	1.641	0.823	1.308	0.883	–	–	–	*− 19.21*
		P2	0.204	0.696	2.209	0.742	1.322	–	–	–	
	(2)	Total	0.185	1.617	0.984	1.094	0.973	0.0782	0.00118	1.0*	− 5.02
		P1	0.184	1.553	0.879	1.326	0.885	0.0623	0.00082	1.0*	− 17.32
		P2	2.039	0.696	2.209	0.742	1.322	0.0000	0.0275	1.0*	

ΔAIC indicates differences from the AIC of baseline model (1) for the entire period. The smallest ΔAIC value for each dataset is indicated in italics. With each threshold magnitude M_c, the first row (indicated "Total" in third column) shows the MLE of the parameters for the entire period ($S = 0.01$, $T_{end} = 2294.52$) until the M6.5 event with AIC = AIC_0. The second row (indicated "P1" in third column) represents the period prior to the change-point ($S = 0.01$, $T_c = 1300$) with AIC = AIC_1. The third row (indicated "P2" in third column) represents the period after the change-point ($T_c = 1300$, $T_{end} = 2294.52$) with AIC = AIC_2. The last column shows $\Delta AIC = AIC_1 + AIC_2 - AIC_0$. The decay rate parameter p_τ for model (2) is fixed to 1.0 in all cases, after Dieterich (1994)

The asterisk symbols indicate that the values are fixed

$t = 1300$ days). Another swarm event in the R5 subregion then followed at around $t = 1700$ days. The changes in $\mu(t)$ in these subregions capture these swarm events well, which suggests that the seismicity in these subregions was likely affected by external forcing, that is, static stress changes and/or fault weakening.

We then analyzed the longer-term seismicity from 1990 until the M6.5 Kumamoto earthquake in Region A (see Fig. 4), including the aftershock sequences in Region B of a strong M5.0 earthquake on June 8, 2000, in the shallower extension of the M6.5 Kumamoto earthquake source (Figs. 4, 6a). Note that the M5.0 earthquake occurred in part of the same fault segment as the M6.5 foreshock on the Hinagu Fault. The mapped faults in the region are generally trend in the east–west or northeast–southwest directions, in agreement with the right-lateral plane of the preliminary focal mechanism and the alignment trends of the early aftershocks. Tables 3 and 4 list the fault parameters and the hypocenter coordinates of the primary focal earthquakes in the Kumamoto region, respectively. Table 5 summarizes the results of the two-stage ETAS model compared with the ordinary ETAS model. The MLEs of the change-points are significant, and the seismicity in Region A and aftershock activity in Region B decreased more than predicted by the corresponding first-stage ETAS models approximately 4 months after the occurrence of the M5.0 mainshock (Fig. 4).

The aftershock activity of the M6.5 Kumamoto earthquake

We next analyzed the aftershock sequence started by the M6.5 earthquake that occurred at 21:26 on April 14, 2014, including the largest aftershock of M6.4 that occurred at 00:03 on April 15, prior to the M7.3 earthquake that occurred at 01:25 on April 16. The total time span was approximately 28 h after the M6.5 earthquake (Tables 3, 4). Ogata (2017a, b) assessed the probability that this sequence would be foreshocks of a mainshock with $M \geq 7.0$ as ~ 5% per month.

By applying the ETAS model to this sequence, we found relative quiescence starting soon after the second largest foreshock of M6.4, with AIC differences $\Delta AIC = -7.04$ for the data with $M_c = 1.5$ and $\Delta AIC = -7.94$ for the data with $M_c = 2.0$ (see Table 6). However, in the case of the $M_c = 2.5$ dataset, the change-point becomes less significant even though relative quiescence is clearly observable in Fig. 5. This result may be attributed to the reduced number of the earthquakes in the dataset.

The aftershocks of the Kumamoto earthquake

We then analyzed the aftershock sequence in the 2-week period after the M7.3 mainshock occurrence. Because of

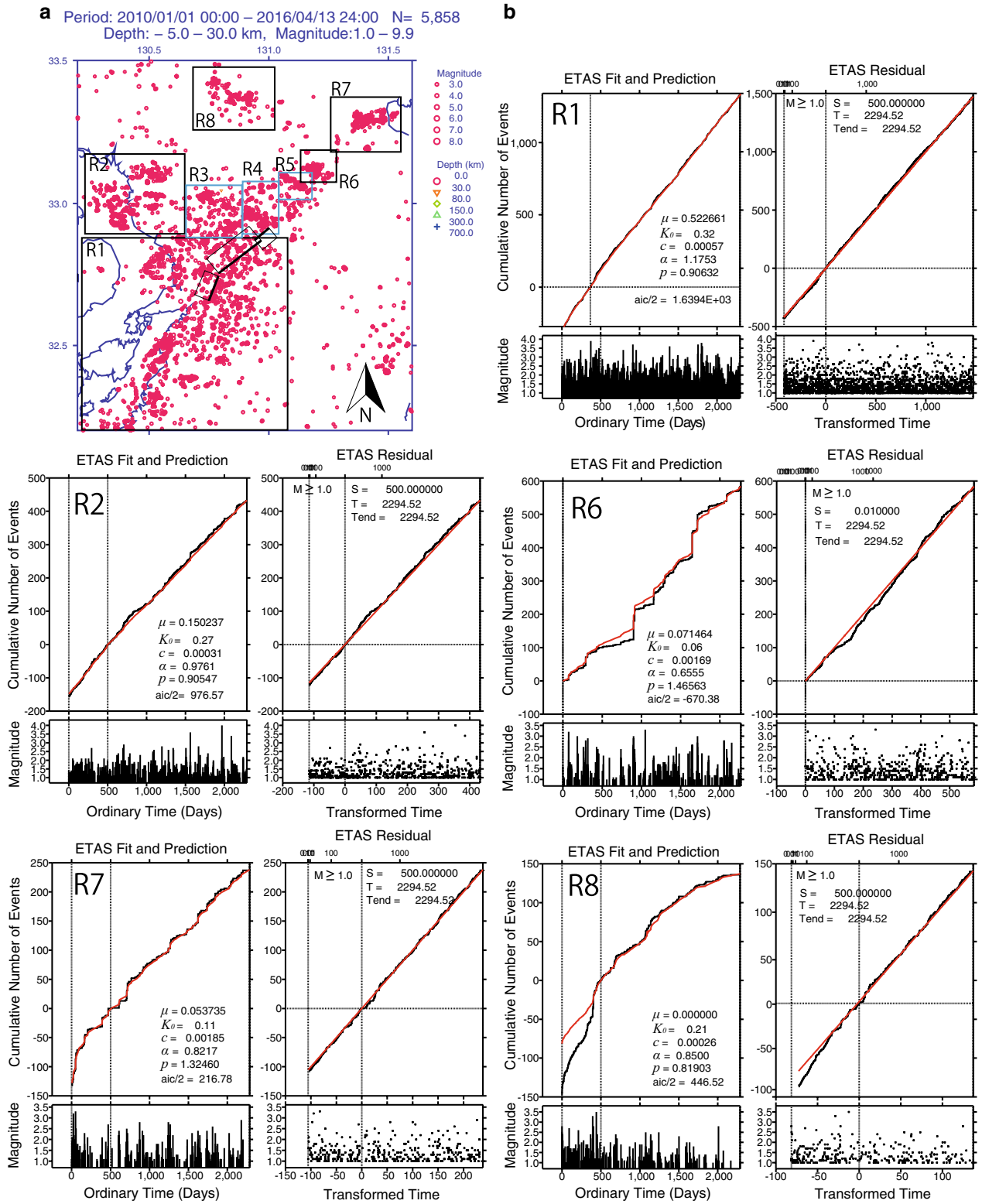

Fig. 2 The ETAS model fitted to the seismicity in the subregions prior to the Kumamoto earthquakes. **a** The total area of Fig. 1a is divided into subregions R1–R8. The thin rectangles indicate the fault models (Geospatial Information Authority of Japan 2016). **b** The ETAS estimate of the cumulative curve (red curve) is superimposed on the observed cumulative curve (black curve) in ordinary time (the left side of each pair) and transformed time (the right side of each pair). The corresponding M–T plots are attached at the bottom of each panel

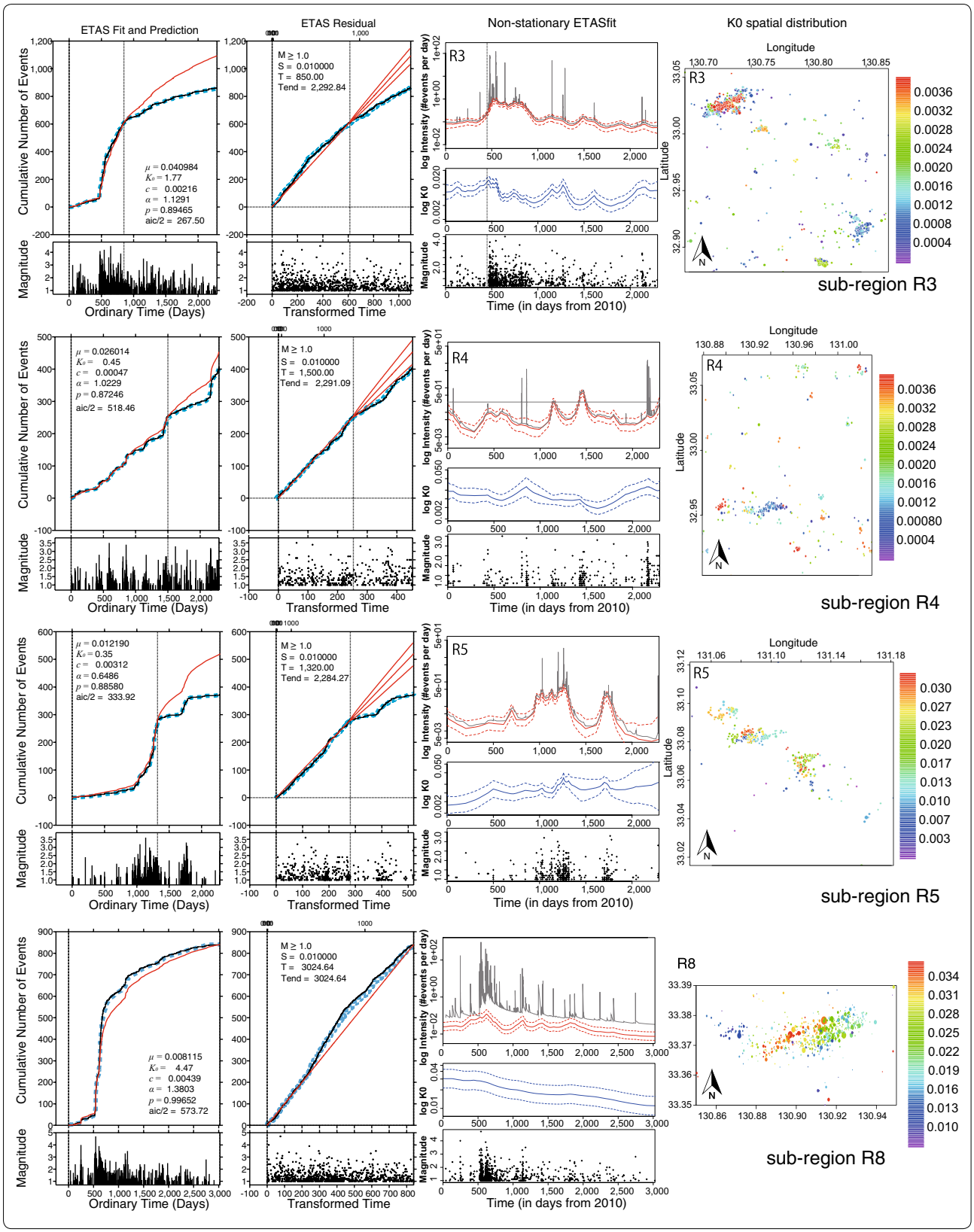
ETAS Fit and Prediction
ETAS Residual
Non-stationary ETASfit
K0 spatial distribution
Cumulative Number of Events
Magnitude
Ordinary Time (Days)
Transformed Time
Time (in days from 2010)
log Intensity (#events per day)
log K0
Longitude
Latitude
R3
R4
R5
R8
sub-region R3
sub-region R4
sub-region R5
sub-region R8

(See figure on previous page.)
Fig. 3 Estimates of ETAS model (1) and non-stationary ETAS model (3). The models are fitted to a seismicity of $M \geq 1.0$ in the R3, R4, R5, and R8 subregions, given from the top to bottom row. The first and second columns show the empirical (black) and theoretical (red) cumulative curves of the ETAS fitted to the data against the ordinary and transformed times of the ETAS model in the target period prior to the most significant change-point of the two-stage ETAS model. Beneath the empirical cumulative curves, the thick dashed light blue curves indicate the theoretical cumulative curves of the non-stationary ETAS model. The third column shows $\mu(t)$ in red and $K_0(t)$ in blue with twofold errors estimated using non-stationary ETAS model (3). The rightmost panels show the spatial distribution of $K_0(t)$ versus the locations of the earthquakes

Table 2 ETAS model parameters estimated for the subregions

Subregion	Target period	$\mu(\times 10^{-1})$	$K_0(\times 10^{-1})$	$c(\times 10^{-3})$	$\alpha(\times 10^{-1})$	p	ΔAIC ($\Delta ABIC$)
R1	$S = 500$, $T_{end} = 2294.52$	5.227	3.239	0.5716	11.753	0.9063	NA
R2	$S = 500$, $T_{end} = 2294.52$	1.502	2.680	0.3063	9.761	0.9055	NA
R3	$S = 0.01$, $T_{end} = 2294.52$	0.1161	2.904	0.349	5.796	0.912	− 43.62 (− 70.28)
	$S = 0.01$, $T_c = 850$	0.4098	17.67	2.1622	11.29	0.8946	
	$T_c = 850$, $T_{end} = 2294.52$	0.0000	18.49	1.864	13.25	0.9184	
R4	$S = 0.01$, $T_{end} = 2294.52$	0.3081	3.405	0.7071	9.113	0.9329	− 13.35 (− 35.91)
	$S = 0.01$, $T_c = 1500$	0.2601	4.469	0.4727	10.23	0.8725	
	$T_c = 1500$, $T_{end} = 2294.52$	0.1784	2.777	0.7732	8.086	0.9737	
R5	$S = 0.01$, $T_{end} = 2294.52$	0. 1064	4.430	64.40	6.069	1.210	− 28.78 (− 55.33)
	$S = 0.01$, $T_c = 1320$	0.1219	3.547	3.120	6.486	0.8858	
	$T_c = 1320$, $T_{end} = 2294.52$	0.09756	4.667	90.74	6.683	1.294	
R6	$S = 0.01$, $T_{end} = 2294.52$	0.7146	0.5595	1.694	6.555	1.466	NA
R7	$S = 500$, $T_{end} = 2294.52$	0.5373	1.127	1.845	8.217	1.325	NA
R8	$S = 500$, $T_{end} = 2294.52$	0.000	2.121	0.258	8.500	0.8190	(− 49.67)

For the R3–R5 subregions, the first row shows the MLE estimates of the parameters for the entire period between $S = 0.01$ days and $T_{end} = 2294.52$ days with $AIC = AIC_0$, the second row shows those for the pre-change-point period (S, T_c) with $AIC = AIC_1$, and the third row shows those for the post-change-point period (T_c, T_{end}) with $AIC = AIC_2$. The last column shows $\Delta AIC = AIC_1 + AIC_2 - AIC_0$, accompanied in parentheses by the ΔABIC of model (3) from the AIC_0

the rapid occurrences of large events of M6.5, M6.4, and M7.3 within a short period of time (Table 4), the missing rate of small earthquakes is not negligible soon after these occurrences. Before the ETAS model and the non-stationary ETAS model were applied to the dataset, we chose a magnitude threshold above which we could safely expect that the data were collected with sufficient completeness over nearly the entire period.

Therefore, for this sequence, the threshold magnitude M_c can be safely chosen at M3.0 taking into account the level of $m(t) + 3\sigma(t)$ according to estimated model (8) in Fig. 10. The b-value changes stepwise, jumping at the second largest foreshock of M6.4 and at the M7.3 mainshock (see Fig. 10, top panel). These characteristic changes are examined in the next section.

As shown in Fig. 6, the aftershocks are clustered in three distinct regions. Hereafter, we analyze these clusters separately using ETAS model (1) and non-stationary ETAS model (3), in addition to model (2) with the remote triggering effect of the M7.3 mainshock on the off-fault subregions.

The Kumamoto subregion (S1 in Fig. 6a) covers a major part of the foreshock activity since the M6.5 earthquake on April 14 and the majority of the aftershocks of the M7.3 mainshock. The plot of depth versus elapsed transformed time (Fig. 6c) shows that the foreshocks migrated deeper and approached the M7.3 hypocenter. The Aso subregion (S2 in Fig. 6a) was initiated by the M3.9 earthquake at 01:32 on April 16 (0.00484 days after the M7.3 event or 1.17048 days after the M6.5 event). The Oita subregion (S3 in Fig. 6a) was initiated by a M5.7 earthquake at 01:25 on April 16 (0.00038 days after the M7.3 mainshock or 1.16601 days after the first foreshock of the M6.5 event).

For the Kumamoto subregion (S1 in Fig. 6a), the non-stationary ETAS model was applied to the seismicity staring from the M6.5 earthquake, with a discontinuity at the natural change-point at the occurrence time of the M7.3 mainshock (Fig. 7). During the period of foreshock activity, the background seismicity rate $\mu(t)$ and the aftershock productivity $K_0(t)$ both decreased until the M7.3 mainshock. This finding is consistent with relative quiescence

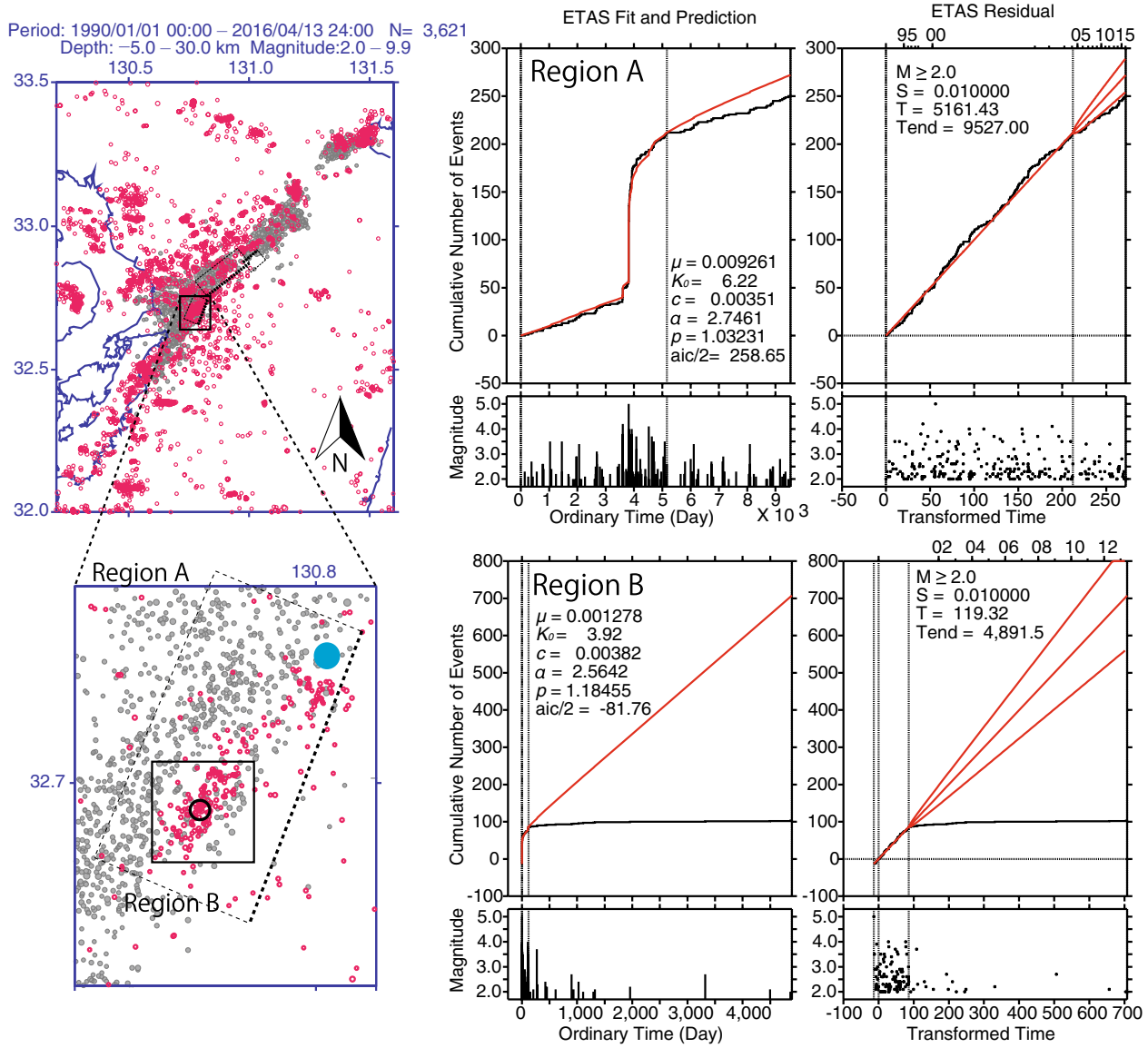

Fig. 4 ETAS model fittings to the restricted regions. ETAS model (1) is fitted to the seismicity in Region A, including the narrow aftershock Region B of the 2000 M5.0 earthquake, beneath which the aftershocks of the 2016 M6.5 and M7.3 Kumamoto earthquakes are plotted as gray circles. The red circles indicate earthquakes from January 1, 1990, until the M6.5 Kumamoto earthquake on April 14, 2016 (blue disk), and its aftershocks prior to the M7.3 mainshock, with a threshold magnitude of $M_c = 2.0$, are plotted as gray circles. The dashed rectangles indicate the fault models of the 2016 Kumamoto earthquakes listed in Table 3. The seismicity in Region B is from 09:32, June 8, 2000, when the mainshock of M5.0 (marked by a thick circle) occurred, and consists only of its aftershocks. The right panels show the ETAS model fitted before the change-point MLE (dashed vertical line) for Region A (top panels) and for the narrower Region B (bottom panels). The estimated cumulative curves are superimposed (red curves) on the observed values (black curves) versus the ordinary time (the left side of each pair) and the transformed time (the right side of each pair). The corresponding M–T plots are attached under the corresponding panels

Table 3 Fault models of the Kumamoto earthquakes (Geospatial Information Authority of Japan 2016)

Fault (Fig. 7)	Lon. (°)	Lat. (°)	Depth (km)	Length (km)	Width (km)	Strike (°)	Dip (°)	Rake (°)	Slip (m)
Left	130.807	32.770	0.8	10.2	13.0	205	72	176	2.7
Middle	130.996	32.878	0.6	20.0	12.5	235	60	209	4.1
Right	130.975	32.883	0.2	5.1	6.6	56	62	178	3.8

Table 4 The occurrence times and epicenter coordinates of the focal earthquakes

Earthquake	Occurrence time	Longitude	Latitude	Depth (km)
M5.0	09:32, June 8, 2000	130.7620°	32.6923°	10.31
M6.5	21:26, April 14, 2016	130.8087°	32.7417°	11.39
M6.4	00:03, April 15, 2016	130.7777°	32.7007°	6.71
M7.3	01:25, April 16, 2016	130.7630°	32.7545°	12.45

Table 5 The MLEs of the single and two-stage ETAS models estimated for Regions A and B in Fig. 4

	Target period	$\mu(\times 10^{-3})$	K_0	$c(\times 10^{-3})$	α	p	ΔAIC
Kumamoto Region A $M_c = 2.0$	$S = 0.01$, $T_{end} = 9527.00$	7.351	5.640	3.280	2.632	1.051	− 3.688
	$S = 0.01$, $T_c = 5161.43$	9.261	6.219	3.507	2.746	1.032	
	$T_c = 5161.43$, $T_{end} = 9105$	8.016	0.050	3.732	2.077	2.059	
Kumamoto Region B $M_c = 2.0$	$S = 0.01$, $T_{end} = 4891.52$	0.4950	5.281	2.233	2.738	1.081	− 3.551
	$S = 0.01$, $T_c = 119.32$	1.279	3.920	3.822	2.564	1.185	
	$T_c = 119.32$, $T_{end} = 4891.52$	0.6071	2.935	1.311	29.20	0.951	

The datasets start at 00:00 on January 1, 1990, and at 10:53 on June 8, 2000 (the occurrence time of a M5.0 event), for Regions A and B, respectively. For each region, the first row shows the MLE estimates of the parameters for the entire period (S, T_{end}) with the associated baseline AIC = AIC_0. The second row for the target period until the change-point (S, T_c) is associated with AIC = AIC_1, and the third row for the target period after the change-point (T_c, T_{end}) is associated with AIC = AIC_2. The last column shows $\Delta AIC = AIC_1 + AIC_2 - AIC_0$

Table 6 MLEs of the single and two-stage ETAS models for the foreshock sequence

	Target period	μ	$K_0(\times 10^2)$	$c(\times 10^{-2})$	$\alpha(\times 10^{-1})$	p	*dAIC*
$M_c = 1.5$	$S = 0.01$, $T_{end} = 1.166$	0.000	2.377	3.166	1.478	1.000	− 7.04
	$S = 0.01$, $T_c = 0.16$	0.000	4.353	9.055	1.516	1.000	
	$T_c = 0.16$, $T_{end} = 1.166$	0.000	1.483	4.492	3.608	1.000	
$M_c = 2.0$	$S = 0.01$, $T_{end} = 1.166$	0.000	1.278	1.878	1.153	1.000	− 7.94
	$S = 0.01$, $T_c = 0.16$	0.000	2.406	6.630	0.9659	1.000	
	$T_c = 0.16$, $T_{end} = 1.166$	0.000	1.273	0.001	1.683	1.000	
$M_c = 2.5$	$S = 0.01$, $T_{end} = 1.166$	0. 000	0.560	0.906	1.119	1.000	− 1.61
	$S = 0.01$, $T_c = 0.16$	0. 000	0.865	0.290	0.913	1.000	
	$T_c = 0.16$, $T_{end} = 1.166$	0. 000	0.291	0.073	0.286	1.000	

Single ETAS model (1) is fitted to the M6.5 aftershock sequence prior to the M7.3 mainshock. For each threshold magnitude, the first row shows the MLEs for the entire period ($S = 0.01$ days, $T_{end} = 1.166$ days) with AIC = AIC_0, the second row shows those for the pre-change-point period ($S = 0.01$ days, $T_c = 0.16$ day) with AIC = AIC_1, and the third row shows those for the post-change-point period ($T_c = 0.16$ days, $T_{end} = 1.166$ days) with AIC = AIC_2. The last column shows $\Delta AIC = AIC_1 + AIC_2 - AIC_0$

in the foreshock series, as discussed in the previous section. In addition, after the M7.3 mainshock, both the background seismicity $\mu(t)$ and the aftershock productivity $K_0(t)$, which had increased, decreased after a few days.

In the Aso subregion (S2 in Fig. 6a), the change-point becomes significant approximately half a day after the M7.3 mainshock ($t = 0.5$ days). The two-stage ETAS model suggests quiescence of the aftershock activity relative to the first period of the induced activity. However, the non-stationary ETAS model fits the dataset better than the two-stage ETAS model (Table 7), showing a moderate decrease in the background seismicity $\mu(t)$ and aftershock productivity $K_0(t)$ (see Fig. 8). The triggering effect due to the static stress changes of the M7.3 mainshock is significant (Table 8), which effect appears closely comparable with the changes in the background seismicity in the non-stationary ETAS model as shown by the green and red curves in Fig. 8. However, the background seismicity decayed faster. It is expected that the causes of the inducement involve fault weakening, not just triggering by the static stress change.

In the Oita subregion (S3 in Fig. 6a), an M5.7 earthquake appears to be induced 32 s after the M7.3 mainshock, which ruptured at a distance of approximately 100 km; then, its aftershocks continued. However, the direct triggering influence from the mainshock on this aftershock activity was weak (Table 8). Quiescence was significant (Table 7) because no earthquakes of M3 or larger occurred for nearly 1 year from approximately

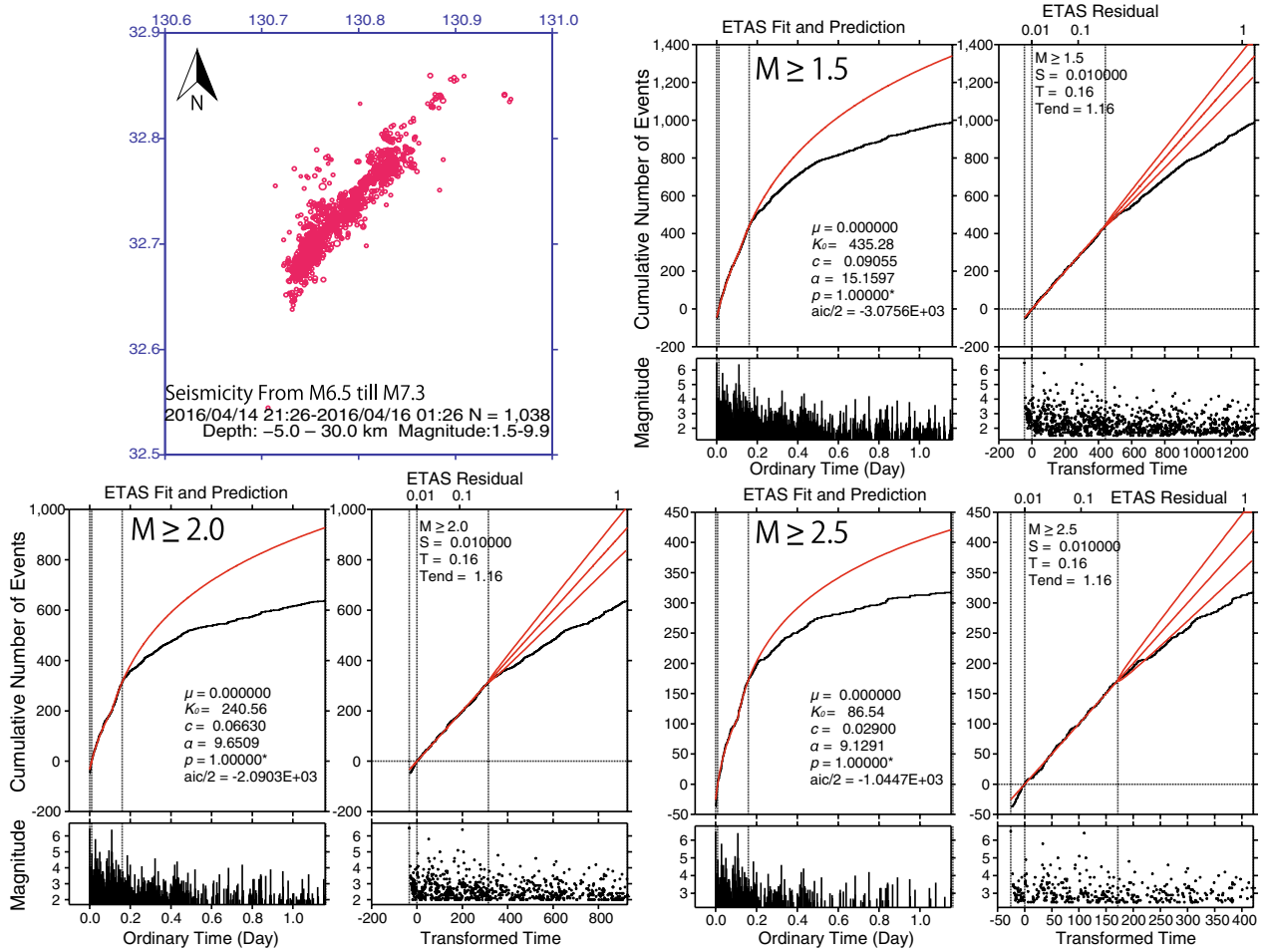

Fig. 5 ETAS model fitted to the foreshock sequence. ETAS model (1) is applied to the aftershock sequence of the M6.5 earthquake prior to the occurrence of the M7.3 mainshock, plotted against the ordinary and transformed times via the theoretical cumulative curve of the ETAS model. The red theoretical cumulative curves are superimposed on the black empirical cumulative curves of the aftershocks of $M \geq 1.5$, $M \geq 2.0$, and $M \geq 2.5$ together with the corresponding M–T diagrams

2 weeks after the mainshock ($t = 15$ days). When the non-stationary ETAS model is applied, the background seismicity and aftershock productivity both show decreasing trends, as shown in Fig. 9. There is little difference between the ETAS model with a change-point and the non-stationary ETAS model. Therefore, future long-term monitoring is necessary. Note that it is not very unusual in this subregion for no events of M3 or larger to be observed for more than 1 year, as shown in the catalog for the past few decades, regardless of the high activity.

Variation in the magnitude frequencies of the foreshocks and aftershocks

The time-dependent model for detection-rate changes combined with *b*-value changes defined in Model and Methods section was applied to all of the compiled events with magnitudes given in the Hypocenter Catalog of the JMA for the 5-day period after the M6.5 event. The 50% detection rates are nearly identical between M2 and M3, but only within a very short period after the M7.3 mainshock (see Fig. 10).

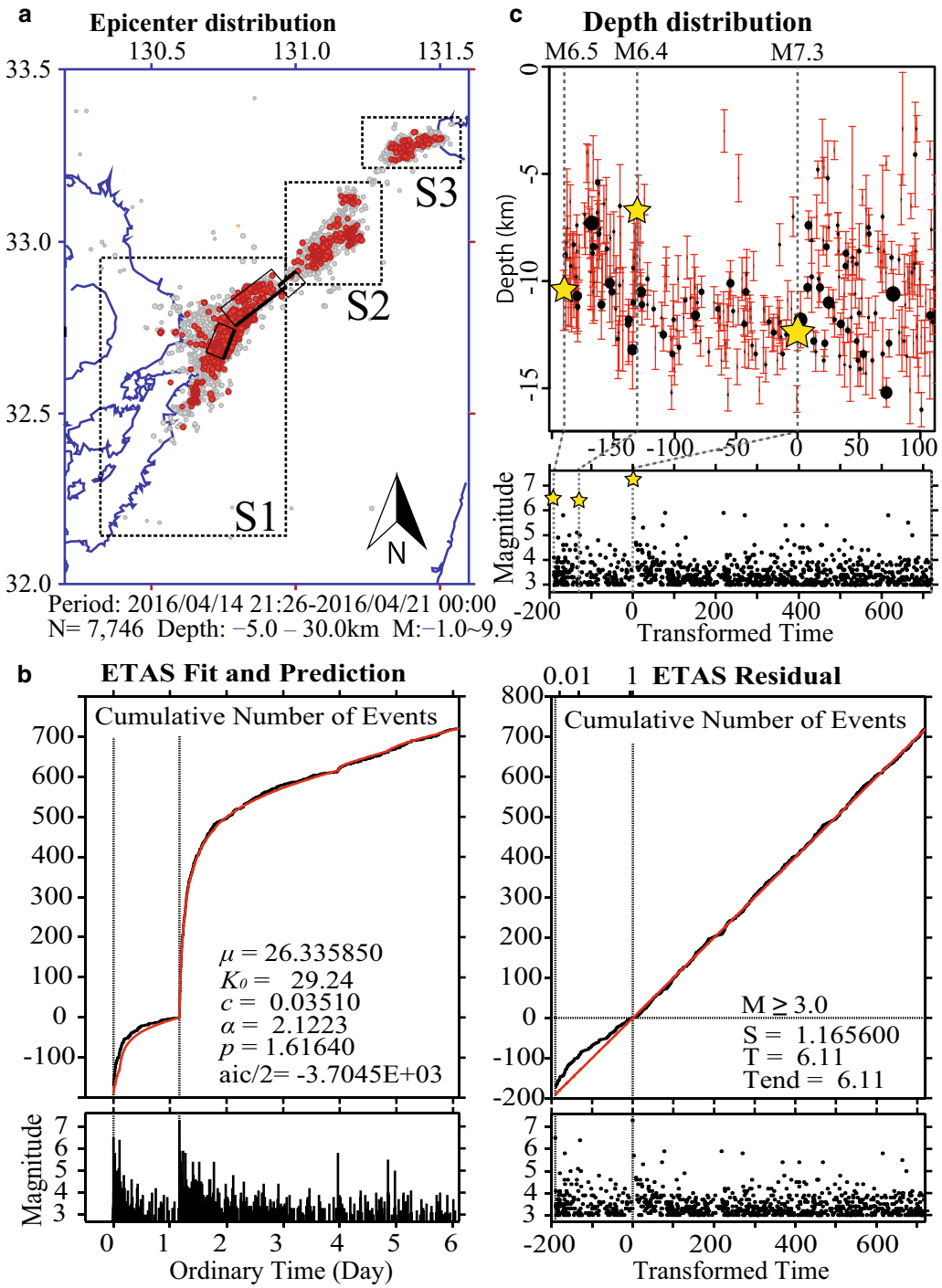

Fig. 6 Epicenter distribution, ETAS model estimate, and depth versus time plots of the foreshocks and aftershocks. **a** The epicenter distribution, where gray disks indicate events with magnitudes less than M3 and red disks indicate those larger than M3. The small rectangles indicate the fault models of the M6.5 and M7.3 ruptures (see Table 3). **b** The results of the ETAS model fitted to the above threshold ($M_c = 3$) dataset of the entire region (red dots in **a**)), where data in the target interval are after the M7.3 mainshock. **c** The depth distribution of earthquakes in region S1 versus the transformed time. The vertical bars indicate the error bounds of the hypocenter depths. The stars indicate the earthquakes of magnitudes 6.5, 6.4, and 7.3 from left to right

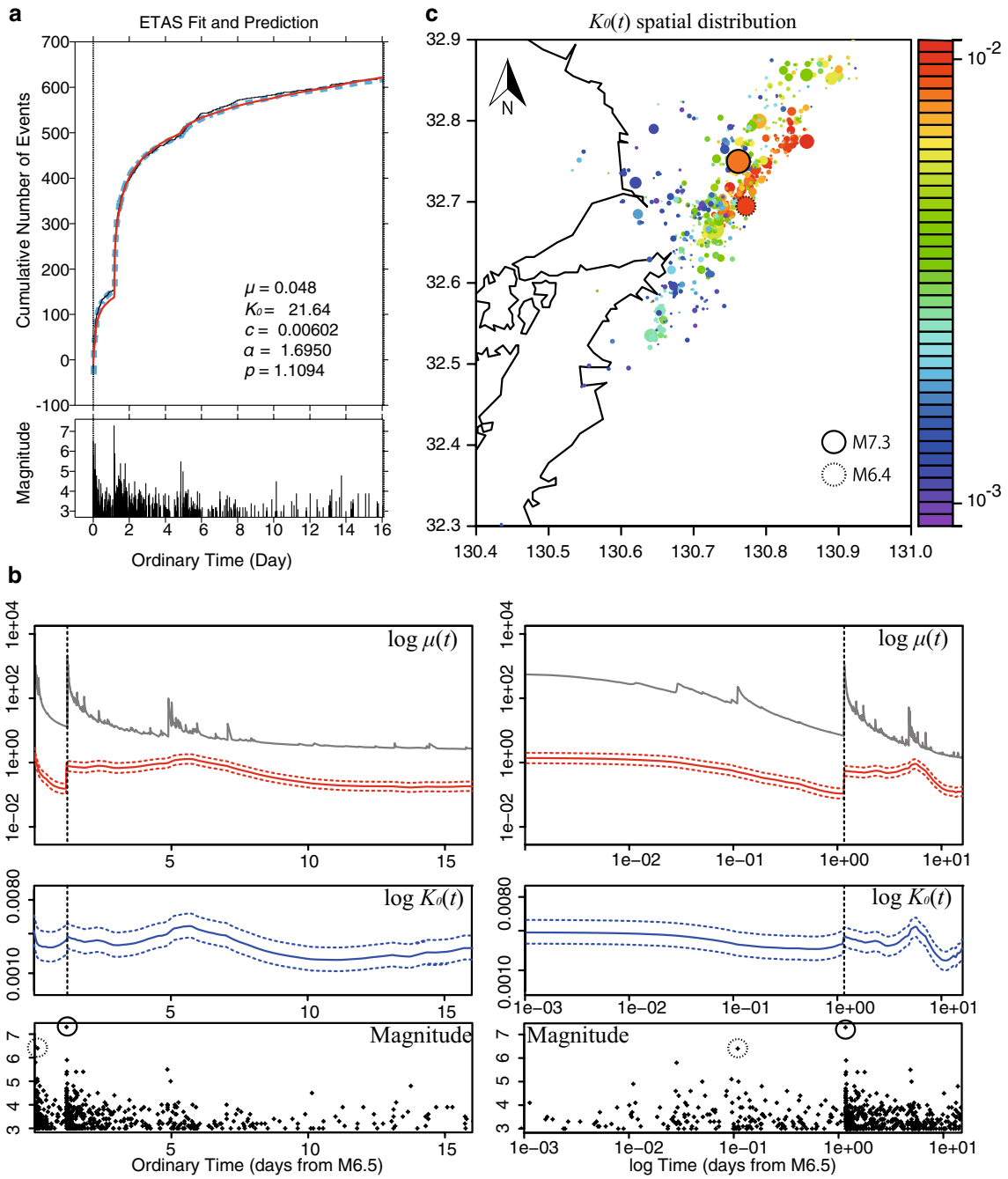

Fig. 7 Non-stationary ETAS model applied to the Kumamoto region (S1 in Fig. 6a). **a** The red cumulative curve indicates the ETAS model fitted for the entire period. The thick dotted light blue curve indicates the estimated non-stationary ETAS model. **b** The estimated time-dependent parameters of the non-stationary ETAS model, where the reference parameters are the MLE of the ETAS model. The MLEs are printed in (**a**). The time axes are on an ordinary scale (left side panel) and a logarithmic scale (right side panel). The vertical dashed line indicates the occurrence time of the M7.3 mainshock. In the M–T plots, the M6.4 and M7.3 events are marked by circles. **c** The estimates of the K_0 parameters versus the corresponding locations of the aftershocks, where the color table shows the expected number of triggering offspring events of $M \geq 3.0$ per square degree per day

Table 7 Model comparisons between the two-stage ETAS model and the non-stationary ETAS model

ΔAIC or ΔABIC	S1	S2	S3
Change-point T_c (ΔAIC)	− 6.99 ($T_c = 1.1656$)	− 9.04 ($T_c = 21$)	− 6.26 ($T_c = 14.9$)
Non-stationary ETAS (ΔABIC)	− 17.58	− 15.11	− 7.03

The differences in the AIC value of the two-stage ETAS model and ABIC value of the non-stationary ETAS model from the AIC of the reference ETAS model are listed. The AIC of the baseline ETAS model is the same as the ABIC of the reference ETAS model. These values are estimated for the entire period for the target region; T_c corresponds to the natural change-point at the occurrence time of the M7.3 mainshock, and days are counted from the occurrence time of the M6.5 foreshock event

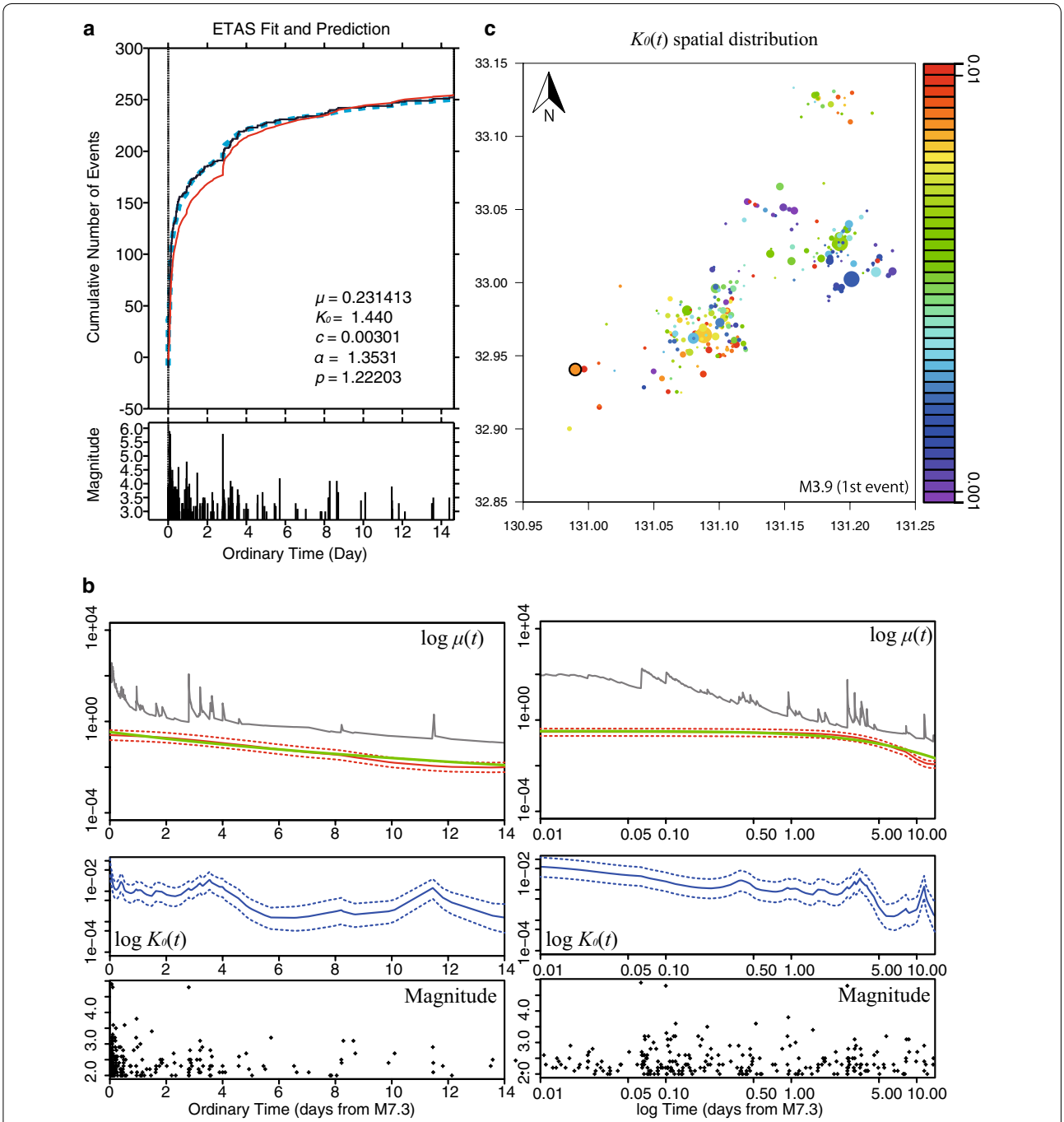

Fig. 8 Non-stationary ETAS model and model (2) applied to the Aso subregion (S2 in Fig. 6a). The marks, line types, and colors are the same as indicated in Fig. 7, except that the thick green curve represents the triggering effect of the M7.3 mainshock indicated by the third term in model (2)

Table 8 Model comparisons between the ETAS model with and without the triggering effect

	μ	K_0	C	A	P	$K_{M7.3}$	$c_{M7.3}$	$P_{M7.3}$	ΔAIC
S2 ETAS	0.0231	1.440	0.00301	1.353	1.222	–	–	–	− 5.23
S2 Equation 2	0.0170	2.494	0.0196	1.586	1.301	0.130	0.153	1.391	
S3 ETAS	0.00561	5.381	0.0257	4.187	1.573	–	–	–	+ 2.51
S3 Equation 2	0.00531	5.072	0.0251	3.031	1.244	1.04×10^{-4}	0.380	1.520	

The MLEs of the reference ETAS model and the ETAS model with triggering effect (Eq. (2)) are listed with the AIC differences between the two models

The *b*-values throughout the foreshock–aftershock sequence of the Kumamoto earthquakes showed step-like changes with a jump at each large event (i.e., the M6.4 and M7.3 events). To explain these changes, we examined the spatial distribution of *b*-values (Fig. 11) estimated from the entire sequence of foreshocks and aftershocks with a cutoff magnitude of $M_c = 2.95$. The foreshocks (white and red dots in Fig. 11) were concentrated in areas where the *b*-value was estimated to be low, whereas the aftershocks (black dots in Fig. 11) were widely dispersed in the high *b*-value area. This migrating epicenter distribution resulted in the second stepwise change of the *b*-value, which jumps at the occurrence of the M7.3 event in Fig. 10. Note here that smoothing constraints were imposed not to the integration of square differentials of the values in time but to the sums of the square differences of the sequential values of consecutive earthquakes. The foreshocks prior to (white dots in Fig. 11) and after the M6.4 event (red dots in Fig. 11) are spread almost equally in the NE–SW direction (distributed around the X–Y line in Fig. 11); however, the former foreshocks are systematically distributed deeper (blue crosses in Fig. 12b) than the latter (red crosses in Fig. 12b), even with estimation errors taken into account. Because the high *b*-value area is located in a deeper zone in the plane along the X–Y line, the latter foreshocks have relatively high *b*-values on average. This finding explains the first stepwise change in the *b*-value in Fig. 10, a jump at the occurrence time of the M6.4 event.

Discussion

Compared with the single ETAS model (Figs. 1, 2), the extended ETAS models illustrate anomalous seismicity in the central Kyushu region, including the triggering effect of the 2011 M9 Tohoku earthquake, notably in the narrow R3 region in Fig. 2. Then, earthquake activity appears to subside in the anomalous regions. It is well known that in geothermal regions, crustal materials are more sensitive to dynamic stress perturbations and earthquakes are more easily affected by these perturbations (e.g., Kumazawa and Ogata 2014; Hill and Prejean 2015; Kumazawa et al. 2016a, b).

Miyazawa (2016) and Uchida et al. (2016) reported that the mainshock remotely triggered earthquakes in the Yufuin–Beppu area (subregion S3 in Fig. 6a). Dynamic triggering is often observed in such geothermal and volcanic areas. In this respect, we have quantitatively analyzed this type of off-fault activity. There are various physical mechanisms that operate to trigger earthquakes (Hill and Prejean 2015) either via increased static shear stress or fault weakening by dynamic stresses where crustal fluids are active agents (e.g., Terakawa 2014; Aiken and Peng 2014). In this respect, we have quantitatively estimated how the background rate of the non-stationary ETAS model fluctuated on the northern side of the focal fault segments of the Kumamoto earthquakes, as shown in Fig. 3.

By applying the two-stage ETAS model to the series of foreshocks led by the M6.5 event, we predicted relative quiescence soon after the M6.4 earthquake until the M7.3 mainshock. Therefore, we expect that the intermediate-term probability gains of predicting large earthquakes of similar size or larger will increase in the vicinity of a large earthquake (Ogata 2001, 2005, 2017a, b).

With the dataset for the first 2 weeks after the M7.3 Kumamoto earthquake, we demonstrated that the

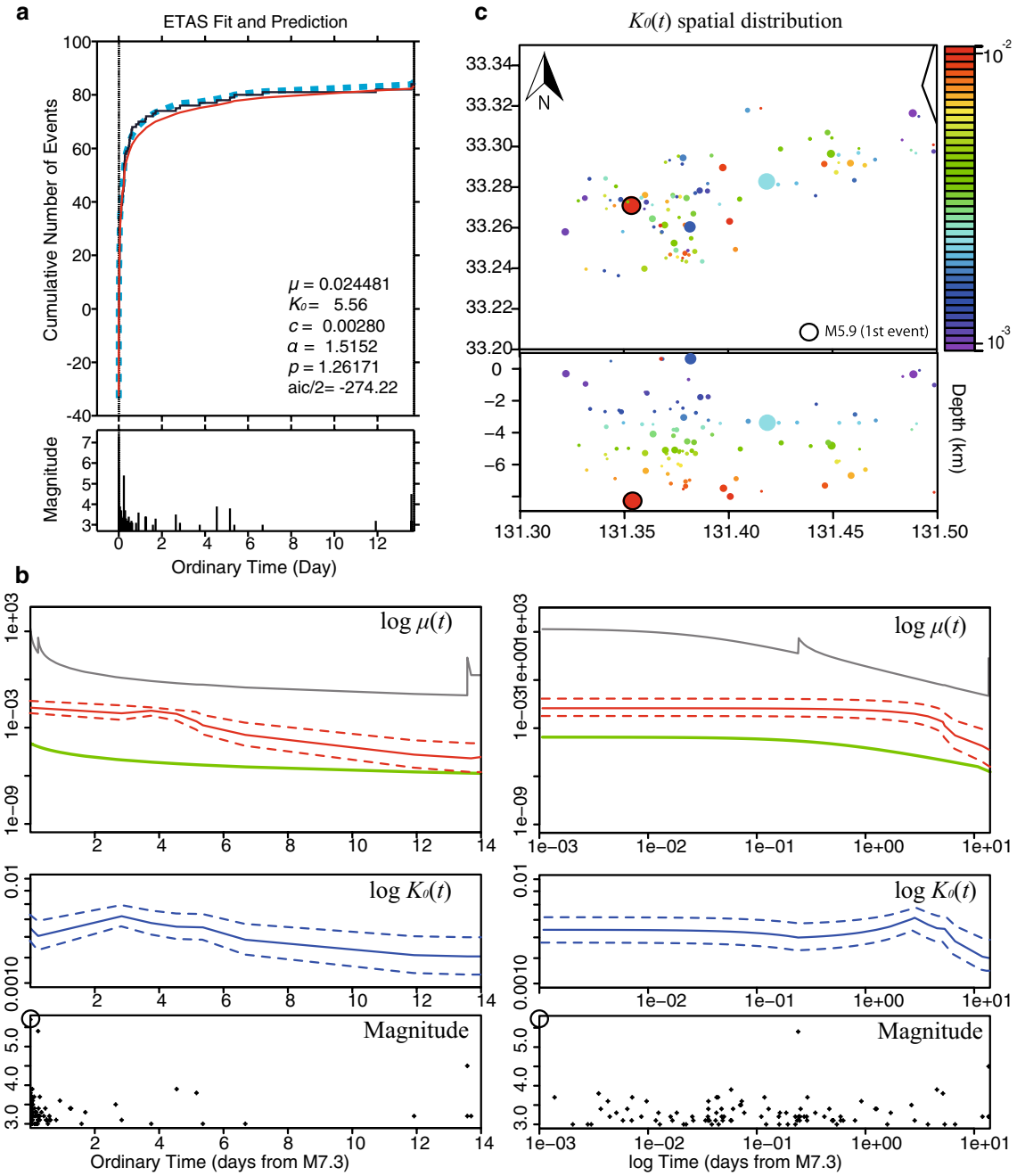

Fig. 9 Non-stationary ETAS model and model (2) applied to the Oita subregion (S3 in Fig. 6a). The marks, line types, and colors are the same as indicated in Fig. 7, except that the thick green curve represents the triggering effect of the M7.3 mainshock indicated by the third term in model (2)

background seismicity rates and the aftershock productivity rates were both decreasing in all subclusters of the aftershock region. For the Aso subregion (S2 in Fig. 6a) and the Oita subregion (S3 in Fig. 6a), the rates of decrease were higher than those of the off-fault static triggering effect expected based on the Omori–Utsu law

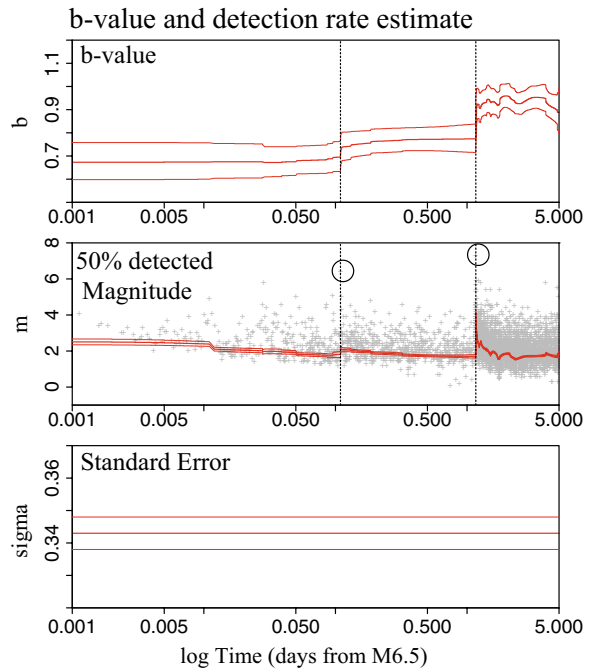

Fig. 10 Earthquake detection-rate parameters and *b*-value estimates. The panels show, from top to bottom, the *b*-value time change and the detection-rate parameters with double error (95%) envelopes versus time on a logarithmic scale. The vertical dashed lines show the occurrence times of the M6.4 and M7.3 earthquakes, which are marked by large circles

in model (2). This finding may be attributed to an end of the fault weakening caused by underground water intrusion resulting from disturbances associated with a sequence of earlier large earthquakes. In particular, for the Oita subregion (S3 in Fig. 6a), the M3.0 and larger events ceased 2 weeks after the mainshock and have been absent for more than a year. However, we cannot yet exclude the possibility of relative quiescence due to the static stress shadow caused by a potential neighboring slow slip event and, therefore, we must continually observe the transitions of the aftershocks. Further continual observation will allow us to identify whether quiescence in this region is a significant anomaly compared with the pattern of earthquake occurrences during a longer time span.

The results presented in Figs. 6c and 12 require homogenous quality of the hypocenter locations, including their depths. The locations and corresponding error estimates for the shallow inland regions in the JMA Hypocenter Catalog (JMA 2017) were determined using the records of the nearest 7–20 stations (typically 20). The hypocenter determination of the JMA catalog was improved significantly in inland regions after October 1997. The JMA now uses a modified shallow one-dimensional velocity model called the JMA2001 travel-time table (see Ueno et al. 2002). Hypocenters are determined by averaging travel-time data adjusted based on several explosion seismic experiments conducted in various inland regions and an improved weighting function continuous on the distance to the hypocenter, and are appropriate for the dense joint seismic networks of the JMA, the Hi-net system of National Research Institute for Earthquake Science and Disaster Resilience, and universities. See Funasaki and Earthquake Prediction Information Division (2004) for the revised JMA magnitudes of smaller earthquakes less than about M5, which are dominant in estimating the current *b*-value.

Conclusions

The increase in the probability gain of a future large earthquake in the vicinity of an aftershock region may be elevated based on the presence of relative quiescence in the aftershock sequence (Ogata 2017a, b). Therefore, it is important to monitor and evaluate the existence of relative quiescence in a focal region.

Ordinary ETAS model (1) fits the microseismicity well in many subregions in the Kumamoto district for data from 2010 until the 2016 Kumamoto earthquake occurrences. The exceptions are swarm-like activities that are quantitatively characterized by the time-dependent background rates of ETAS model (3). Another slight change in seismicity rate includes the induced effect of the 2011 M9.0 Tohoku-Oki mega-earthquake.

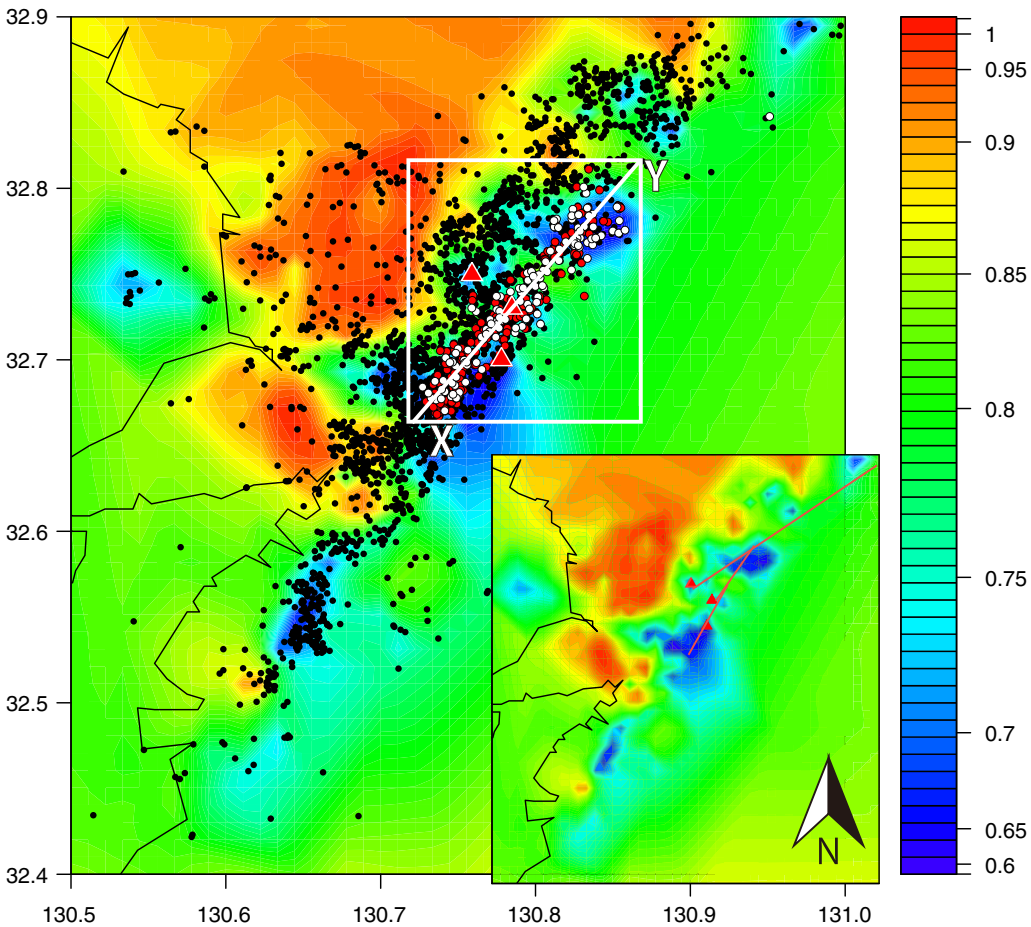

Fig. 11 The horizontal changes in *b*-value. The white and red dots represent the epicenters of the foreshocks before and after the M6.4 event, respectively, and the black dots represent the epicenters of the aftershocks. The red triangles indicate the epicenters of the M6.4, M6.5, and M7.3 earthquakes from south to north. The red segments indicate simplified traces of the Hinagu Fault and the Futagawa Fault from south to north (see Table 3 for the fault parameters). The inset panel shows only the *b*-value image

We applied two-stage ETAS models to seismic activity data for the subregions where the stationary ETAS model showed significant misfits. In particular, relative quiescence was detected in the sequences led by the M6.5 event and another precursory sequence led by the 2000 M5.0 event in the shallower proximate zone of the M6.5 event. In addition, the foreshocks led by the M6.5 event migrated deeper to approach the M7.3 hypocenter (Fig. 6c).

We further applied ordinary ETAS model (1), non-stationary ETAS model (3), and the model of *b*-value change estimate (model (8)) to the sequence throughout the M6.5 foreshocks and the aftershocks of the M7.3 event for the first 2-week period.

We closely examined the aftershock activity that followed the M7.3 event in the main Kumamoto subregion and regionally separated two off-fault zones. In all regions evaluated, the background seismicity rate $\mu(t)$ and the aftershock productivity $K_0(t)$ both gradually decreased and decreased faster than the rates assumed based on the static triggering effect from the M7.3 mainshock. Therefore, we expect that fluid intrusion and diffusion, in addition to the static triggering effect, were involved in triggering aftershocks in the early period.

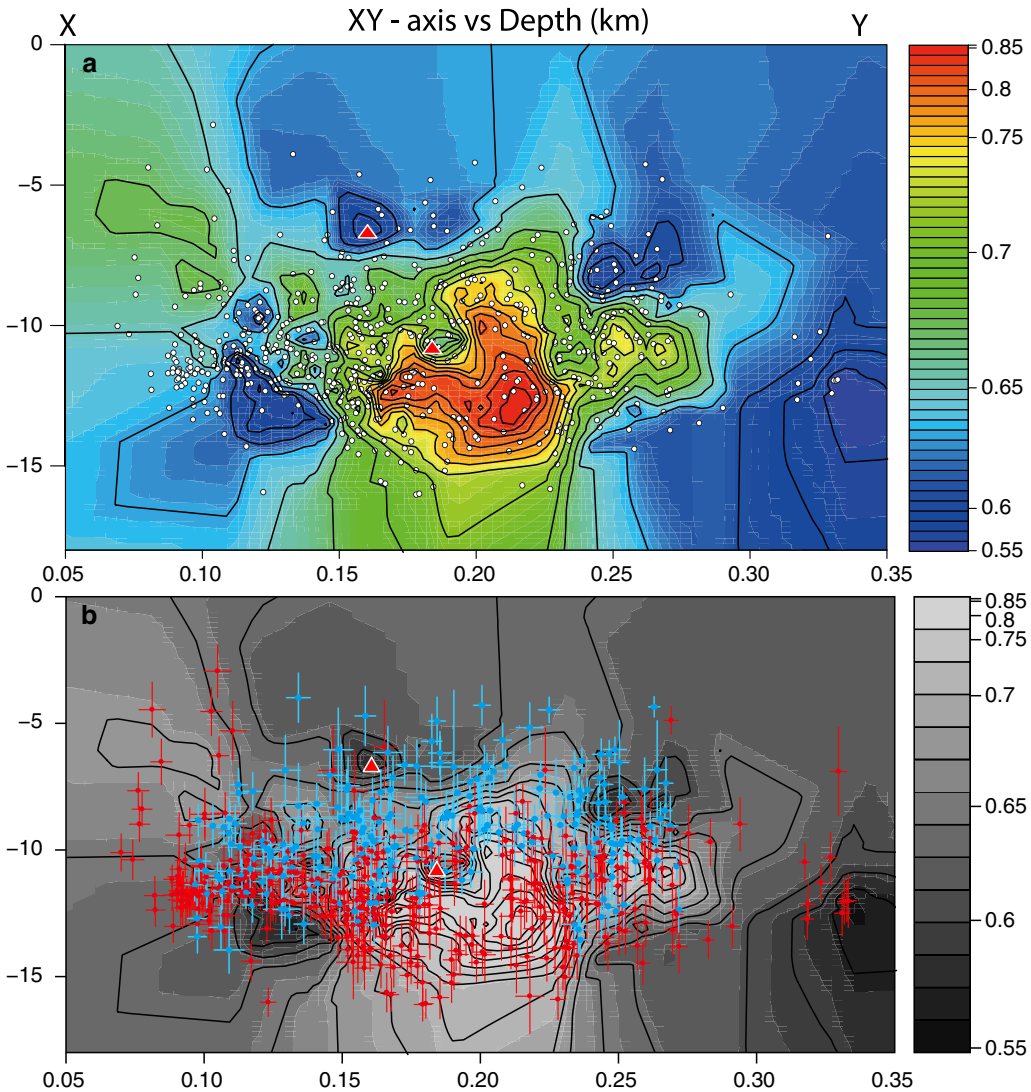

Fig. 12 The vertical *b*-value variation of foreshocks. **a** The white dots represent the hypocenters of the foreshock sequence projected onto the X–Y lateral plane (in Fig. 11). Colors and contours show the *b*-value distribution. The contours are in increments of 0.02. Red triangles indicate the hypocenters of the M6.5 and M6.4 earthquakes in order from the shallow side. **b** Blue dots with error bars represent the hypocenters of the foreshocks prior to the M6.4 foreshock, and red dots with error bars represent the hypocenters of the foreshocks after the M6.4 event

The *b*-value increased stepwise over time, with jumps at the major M6.5, M6.4, and M7.3 events. In this case, these seemingly time-dependent *b*-value changes can be explained by the regional *b*-value difference and the migration of seismic activity.

Abbreviations

AIC: Akaike information criterion; ABIC: Akaike Bayesian information criterion; ETAS model: epidemic-type aftershock sequence model; MLE: maximum likelihood estimate; RPP: residual point process; XETAS: X-windows-based ETAS applications.

Authors' contributions

YO organized the study and prepared the original statistical programs for the methods. HT wrote the XETAS programs and modified and extended the functions for the current study. TK modified and arranged the statistical tools, carried out the analysis, and drafted the manuscript. YO and HT checked the results and manuscript. All authors read and approved the final manuscript.

Author details

[1] The Institute of Statistical Mathematics, Tachikawa, Japan. [2] Earthquake Research Institute, University of Tokyo, Tokyo, Japan.

Acknowledgements

We are grateful for the support from the Japan Society for the Promotion of Science KAKENHI Grant 16K00065 and 17H00727. This paper has been improved by constructive comments from anonymous reviewers.

Competing interests

The authors declare that they have no competing interests.

Ethics approval and consent to participate
The authors declare that they have no competing interests.

Publisher's Note

Received: 23 August 2017 Accepted: 6 December 2017
Published online: 21 December 2017

References

Aiken C, Peng Z (2014) Dynamic triggering of microearthquakes in three geothermal/volcanic regions of California. J Geophys Res 119:6992–7009. https://doi.org/10.1002/2014JB011218
Akaike H (1973) Information theory and an extension of the maximum likelihood principle. In: Petrov BN, Csaki F (eds) Proceedings of 2nd international symposium on information theory. Akademiai Kiado, Budapest, pp 267–281
Akaike H (1980) Likelihood and Bayes procedure. In: Bernard JM, De Groot MH, Lindley DU, Smith AFM (eds) Bayesian statistics. University Press, Valencia
Akaike H (1992) Information theory and an extension of the maximum likelihood principle. Republished Edition. In: Kotz S, Johnson NL (eds) Breakthroughs in statistics, vol I, foundations and basic theory. Springer, New York, pp 610–624
Aki K (1965) Maximum likelihood estimate of b in the formula log; N = a-bM and its confidence limits. Bull Earthq Res Inst Univ Tokyo 43:237–239
Dieterich J (1994) A constitutive law for rate of earthquake production and its application to earthquake clustering. J Geophys Res 99:2601–2618
Funasaki J, Earthquake Prediction Information Division (2004) Revision of the JMA velocity magnitude (in Japanese). Quart J Seis 67:11–20
Good IJ, Gaskins RA (1971) Nonparametric roughness penalties for probability densities. Biometrika 58:255–277
Gutenberg R, Richter CF (1944) Frequency of earthquakes in California. Bull Seismol Soc Am 34:185–188
Hainzl S, Ogata Y (2005) Detecting fluid signals in seismicity data through statistical earthquake modeling. J Geophys Res 110:B05S07. https://doi.org/10.1029/2004JB003247
Hill DP, Prejean S (2015) Dynamic triggering. In: Kanamori H (ed) Treatise on geophysics, 2nd edn, vol 4. Elsevier, Amsterdam, pp 273–304
JMA (2017) The seismological bulletin of Japan. http://www.data.jma.go.jp/svd/eqev/data/bulletin/index_e.html
Kumazawa T, Ogata Y (2013) Quantitative description of induced seismic activity before and after the 2011 Tohoku-Oki Earthquake by non-stationary ETAS models. J Geophys Res 118:6165–6182
Kumazawa T, Ogata Y (2014) Nonstationary ETAS models for nonstandard earthquakes. Ann Appl Stat 8(3):1825–1852. https://doi.org/10.1214/14-aoas759
Kumazawa T, Ogata Y, Toda S (2010) Precursory seismic anomalies and transient crustal deformation prior to the 2008 Mw = 6.9 Iwate-Miyagi Nairiku, Japan, earthquake. J Geophys Res 115:B10312. https://doi.org/10.1029/2010JB007567
Kumazawa T, Ogata Y, Kimura K, Maeda K, Kobayashi A (2016a) Background rates of swarm earthquakes that are synchronized with volumetric strain changes. Earth Planet Sci Lett 442:51–60. https://doi.org/10.1016/j.epsl.2016.02.049
Kumazawa T, Ogata Y, Tsuruoka H (2016b) Statistical monitoring of seismicity in Kyushu District before the occurrence of the 2016 Kumamoto earthquakes of M6.5 and M7.3. Rep Coord Comm Earthq Predic 96. http://cais.gsi.go.jp/YOCHIREN/report/index96.html
Matsu'ura RS (1986) Precursory quiescence and recovery of aftershock activities before some large aftershocks. Bull Earthq Res Inst Univ Tokyo 61:1–65
Miyazawa M (2016) An investigation into the remote triggering of the Oita earthquake by the 2016 Mw 7.0 Kumamoto earthquake using full wavefield simulation. Earth Planets Space 68:205. https://doi.org/10.1186/s40623-016-0585-z
Nanjo KZ, Izutsu J, Orihara Y, Furuse N, Togo S, Nitta H, Okada T, Tanaka R, Kamogawa M, Nagao T (2016) Seismicity prior to the 2016 Kumamoto earthquakes. Earth Planets Space 68:190. https://doi.org/10.1186/s40623-016-0558-2
Ogata Y (1978) The asymptotic behavior of maximum likelihood estimator of stationary point processes. Ann Inst Stat Math 30:243–261
Ogata Y (1985) Statistical models for earthquake occurrences and residual analysis for point processes, Research Memorandum (Technical report) No 288, and also in *Suri-Zisin Gaku* (*Mathematical Seismology*), vol 1, Saito M (ed), Cooperative Research Report, March 1986. The Institute of Statistical Mathematics, Tokyo
Ogata Y (1988) Statistical models for earthquake occurrences and residual analysis for point processes. J Am Stat Assoc 83:9–27
Ogata Y (1989) Statistical model for standard seismicity and detection of anomalies by residual analysis. Tectonophysics 169:159–174
Ogata Y (1992) Detection of precursory relative quiescence before great earthquakes through a statistical model. J Geophys Res 97:19845–19871
Ogata Y (2001) Increased probability of large earthquakes near aftershock regions with relative quiescence. J Geophys Res 106:8729–8744
Ogata Y (2005) Detection of anomalous seismicity as a stress change sensor. J Geophys Res 110:B05S06. https://doi.org/10.1029/2004JB003245
Ogata Y (2006a) Statistical Analysis of Seismicity: updated version (SASeis2006) Ver. 2, Computer Science Monographs No. 33, The Institute of Statistical Mathematics, Tokyo. http://www.ism.ac.jp/~ogata/Ssg/ssg_softwares.html
Ogata Y (2006b) Monitoring of anomaly in the aftershock sequence of the 2005 earthquake of M7.0 off coast of the western Fukuoka, Japan, by the ETAS model. Geophys Res Lett 33(1):L01303. https://doi.org/10.1029/2005GL024405
Ogata Y (2007) Seismicity and geodetic anomalies in a wide area preceding the Niigata-Ken-Chuetsu earthquake of 23 October 2004, central Japan. J Geophys Res 112:B10301. https://doi.org/10.1029/2006JB004697
Ogata Y (2011a) Pre-seismic anomalies in seismicity and crustal deformation: case studies of the 2007 Noto Hanto earthquake of M6.9 and the 2007 Chuetsu-oki earthquake of M6.8 after the 2004 Chuetsu earthquake of M6.8. Geophys J Int 186:331–348
Ogata Y (2011b) Significant improvements of the space-time ETAS model for forecasting of accurate baseline seismicity. Earth Planets Space 63(3):217–229. https://doi.org/10.5047/eps.2010.09.001
Ogata Y (2017a) Forecasting of a large earthquake: an outlook of the research. Seismol Res Lett 88(4):1117–1126. https://doi.org/10.1785/0220170006
Ogata Y (2017b) Statistics of Earthquake Activity: models and methods for earthquake predictability studies. Annu Rev Earth Planet Sci 45:497–527. https://doi.org/10.1146/annurev-earth-063016-015918
Ogata Y (2017c) On consecutive seismicity rate in Japanese inland. Rep Coord Comm Earthq Predict 97:9–12. http://cais.gsi.go.jp/YOCHIREN/report/kaihou97/1_3.pd
Ogata Y, Katsura K (1993) Analysis of temporal and spatial heterogeneity of magnitude frequency distribution inferred from earthquake catalogues. Geophys J Int 113:727–738
Ogata Y, Katsura K (2006) Immediate and updated forecasting of aftershock hazard. Geophys Res Lett 33(10):L10305
Ogata Y, Tsuruoka H (2016) Statistical monitoring of aftershock sequences: a case study of the 2015 Mw7.8 Gorkha, Nepal, earthquake. Earth Planets Space 68(44):2016. https://doi.org/10.1186/s40623-016-0410-8
Ogata Y, Imoto M, Katsura K (1991) 3-D spatial variation of *b*-values of magnitude-frequency distribution beneath the Kanto District, Japan. Geophys J Int 104:135–146
Ogata Y, Utsu T, Katsura K (1995) Statistical features of foreshocks in comparison with other earthquake clusters. Geophys J Int 121:233–254
Ogata Y, Utsu T, Katsura K (1996) Statistical discrimination of foreshocks from other earthquake clusters. Geophys J Int 127:17–30
Ogata Y, Katsura K, Tanemura M (2003) Modelling heterogeneous space-time occurrences of earthquakes and its residual analysis. Appl Stat (JRSSC) 52(4):499–509
Parzen E, Tanabe K, Kitagawa G (eds) (1998) Selected papers of Hirotugu Akaike. Springer, Tokyo
Ringdal F (1975) On the estimation of seismic detection thresholds. Bull Seismol Soc Am 65:1631–1642
Smith WD (1986) Evidence for precursory changes in the frequency magnitude *b*-value. Geophys J R Astron Soc 86:815–838

Terakawa T (2014) Evolution of pore fluid pressures in a stimulated geothermal reservoir inferred from earthquake focal mechanisms. Geophys Res Lett 41:7468–7476

Tsuruoka H (1996) Development of seismicity analysis software on workstation (in Japanese). Tech Res Rep 2:34–42. Earthquake Res Inst, Univ Tokyo, Tokyo

Tsuruoka H, Ogata Y (2015a) Development of seismicity analysis software: TSEIS–ETAS module implementation, 9th International Workshop on Statistical Seismology (StatSei9), Arcona Hotel am Havelufer, Potsdam, Germany, 17 June 2015. https://statsei9.quake.gfz-potsdam.de/doku.php?id=13_presentations:start

Tsuruoka H, Ogata Y (2015b) Development of seismicity analysis tool XETAS, Programme and abstract, the Seismological Society of Japan, 2015, Fall meeting, S09-P01, Kobe, Japan, 26 October 2025: Zisin (II) (Journal of Seismological Society of Japan)

Uchida N, Asano Y, Hasegawa A (2016) Acceleration of regional plate subduction beneath Kanto Japan, after the 2011 Tohoku-oki earthquake. Geophys Res Lett 43:9002–9008. https://doi.org/10.1002/2016GL070298

Ueno H, Hatakeyama S, Aketagawa T, Funasaki J, Hamada N (2002) Improvement of hypocenter determination procedures in the Japan Meteorological Agency: improvement of shallow part velocity structure and weight function. Q J Seismol 65:123–134

Utsu T (1965) A method for determining the value of *b* in a formula log $n = a - bM$ showing the magnitude-frequency relation for earthquakes. Geophys Bull Hokkaido Univ 13:99–103

Utsu T, Ogata Y, Matsu'ura RS (1995) The centenary of the Omori formula for a decay law of aftershock activity. J Phys Earth 43:1–33

Wiemer S, Wyss M (1997) Mapping the frequency-magnitude distribution in asperities: an improved technique to calculate recurrence times? J Geophys Res 102(B7):15115–15128

Wyss M, Shimazaki K, Wiemer S (1997) Mapping active magma chambers by *b*-value beneath the off-Ito volcano. Japan. J Geophys Res 102(20):413–20422